Selective perijunctional MLCK1 recruitment in Crohn's disease: Identification of essential structural domains

Sandra D. Chanez-Paredes[1], Shabnam Abtahi[1], Juanmin Zha[2], Li Zuo[1,3], Weiqi He[2], Jerrold R. Turner[1]

[1]Laboratory of Mucosal Barrier Pathobiology, Department of Pathology, Brigham and Women's Hospital and Harvard Medical School, Boston, MA, USA.

[2]Jiangsu Key Laboratory of Neuropsychiatric Diseases and Cambridge-Suda (CAM-SU) Genomic Resource Center, Soochow University, and Department of Oncology, The First Affiliated Hospital of Soochow University, Suzhou, China.

[3]Anhui Medical University, Hefei, Anhui, China, 230032

Correspondence:
Weiqi He (whe@suda.edu.cn) and Jerrold R. Turner (jrturner@bwh.harvard.edu)

Author contributions: Conceptualization: SC-P, WH, JRT. Experimentation: SC-P, WH. Data analysis SC-P, WH, SA, JZ, LZ, JRT. Manuscript preparation: SC-P, WH, JRT. Manuscript editing: SC-P, WH, SA, JZ, LZ, JRT.

Short title: Mechanisms of MLCK1 recruitment

Competing interests: JRT is a founder of Thelium Therapeutics and a consultant for Entrinsic and Kallyope.

Data sharing: Data that support the findings of this study are included in the main text. Requests for additional information or materials may be addressed to the corresponding author.

Funding: Supported by National Institute of Diabetes and Digestive and Kidney Diseases (R01 DK061931, R01 DK068271, P30 DK034854), Natural Science Foundation of Jiangsu Province (BK20190043), and National Natural Science Foundation of China (31971062).

Classifications: Biological sciences: biochemistry, cell biology, physiology

Keywords: myosin light chain kinase, tight junction, inflammatory bowel disease, intestinal permeability, barrier dysfunction

This PDF file includes:

Main Text: 4846 words (excl. methods and references)
Materials and Methods
47 references
Figures 1 to 7 and legends

ABSTRACT

Intestinal epithelia express two long MLCK splice variants, MLCK1 and MLCK2. We have previously shown that disruption of inflammation-induced MLCK1 recruitment to the perijunctional actomyosin ring prevents barrier loss and attenuates disease progression. Here we sought to define the domains responsible for distinct MLCK1 and MLCK2 behaviors. Quantitative analysis of human biopsies demonstrated specific increases in MLCK1 expression and perijunctional localization in Crohn's disease. When expressed in cultured intestinal epithelial cells, we found, as expected, that MLCK1 is most concentrated at the perijunctional actomyosin ring. In contrast, MLCK2 is predominantly associated with basal F-actin stress fibers. Immunoglobulin-cell adhesion molecule domain 3 (IgCAM3) must be critical for MLCK1 recruitment, as that domain is incomplete in MLCK2. Consistent with this, truncation mutants consisting of N-terminal IgCAM domains 1-4, without C-terminal catalytic domains, localized similarly to full-length MLCK1 and MLCK2, respectively. Further mutagenesis allowed identification of IgCAM2 and IgCAM3 domains as the minimal region required for MLCK1 recruitment. Although IgCAM3 does not concentrate perijunctionally, it can act as a dominant negative effector that limits steady-state and TNF-induced MLCK1 recruitment and barrier loss. Together, the demonstration of selective MLCK1 upregulation and perijunctional recruitment in Crohn's disease and identification of domains required for perijunctional MLCK1 recruitment provide a conceptual understanding and structural data needed for development of therapeutic means of blocking MLCK1-mediated barrier loss without the toxicity of enzymatic MLCK inhibition.

SIGNIFICANCE STATEMENT

Recent work has demonstrated that long myosin light chain kinase isoform 1 (MLCK1) recruitment to the perijunctional actomyosin ring is a critical component of inflammation-induced intestinal barrier loss. Chanez-Paredes *et al.* show that this occurs in Crohn's disease and define the essential structural elements that direct MLCK1 recruitment, thereby creating a foundation for therapeutic interruption of MLCK1 recruitment in disease.

INTRODUCTION

The critical role of MLCK in physiologic and pathologic regulation of intestinal epithelial tight junctions was first reported 20 years ago (1, 2) and, since that time, has been confirmed using in vitro and in vivo models, and in diseased human tissues (3-16). The initial cloning of human intestinal epithelial MLCK demonstrated that long MLCK, but not short, smooth muscle MLCK, was expressed within human intestinal epithelia. Two long MLCK splice variants with distinct, differentiation-dependent expression patterns were detected; MLCK1 was limited to villus epithelia while MLCK2, which lacks exon 11, was expressed throughout the crypt-villus axis (17). The subcellular distributions of these splice variants also differed, with MLCK1 preferentially localized to the perijunctional actomyosin ring (6, 17). More recently, we demonstrated that inflammatory stimuli including tumor necrosis factor (TNF) trigger further MLCK1 recruitment to the perijunctional actomyosin ring in vitro and in vivo (6, 18).

The 69 amino acids encoded by exon 11 complete the third of six immunoglobulin-cell adhesion molecule (IgCAM) domains within the N-terminal extension that differentiates long and short MLCK isoforms. IgCAM3 is, therefore, incomplete in MLCK2. Our recent studies indicate that IgCAM3 is required for steady-state and inflammation-induced MLCK1 recruitment (6, 18) and that disruption of interactions between IgCAM3 and FKBP8 displaces perijunctional MLCK1 and prevents TNF-induced MLC phosphorylation and barrier loss in vitro and in vivo (6).

Although IgCAM3 is required, it is not clear if this domain alone is sufficient to direct perijunctional MLCK1 recruitment. We sought to address this and to determine the structures that mediate steady-state and TNF-induced MLCK1 localization. We identified a region beginning at the end of IgCAM1 through the end of IgCAM3 as the minimal MLCK1 trafficking domain. Although IgCAM3 is distributed diffusely throughout the cytoplasm, it can function as a dominant negative effector that prevents steady-state and TNF-induced MLCK1 recruitment and limits TNF-induced barrier loss. These data expand our understanding of the structures required for the unique subcellular localization of MLCK1 and provide a foundation for development of molecular therapies that interfere with MLCK1 recruitment and prevent inflammation-associated intestinal barrier loss and disease progression.

RESULTS

MLCK1 is upregulated and specifically recruited to the perijunctional actomyosin ring in Crohn's disease

We recently reported that, similar to well-differentiated Caco-2_{BBe} monolayers, TNF increased MLCK1 expression and perijunctional recruitment in human duodenal enteroids (18). To determine if this also occurs in human disease, we analyzed ileal biopsies from Crohn's disease patients and healthy controls by quantitative immunofluorescence using MLCK1-specific or pan-long MLCK antibodies. In controls, MLCK1 was primarily expressed in villus epithelium and concentrated at the perijunctional actomyosin ring and within the apical cytoplasm (Fig. 1A, B). Total long MLCK was present throughout the cytoplasm and on lateral membranes of epithelia throughout the crypt-villus axis but only a minor component was present at the perijunctional actomyosin ring (Fig. 1A, B). Expression of both MLCK1 and total MLCK was significantly increased throughout the crypt-villus axis in Crohn's disease (Fig. 1B, C), and MLCK1 was almost entirely restricted to the perijunctional actomyosin ring (Fig. 1B). Moreover, the magnitude of increased MLCK1 detection in Crohn's disease was significantly greater than that of total MLCK (Fig. 1C), suggesting that inflammatory stimuli bias mRNA splicing towards greater expression of MLCK1. Total long MLCK expression, MLCK1 expression, and MLCK1 recruitment to the perijunctional actomyosin ring are, therefore, all increased in Crohn's disease.

MLCK1 and MLCK2 differentially associate with distinct actin-rich structures

Although we can infer that structures labeled with anti-total MLCK but not anti-MLCK1 reflect MLCK2 localization, the absence of unique sequences present in MLCK2 makes impossible to develop MLCK2-specific antisera. To overcome this, we stably expressed MLCK1-EGFP and MLCK2-EGFP in Caco-2_{BBe} cells and assessed their subcellular localization in well-differentiated epithelial monolayers. When assessed by Western blot using antibodies against total MLCK or EGFP, independent transfected populations demonstrated equivalent expression of MLCK1-EGFP and MLCK2-EGFP (Fig. 2A). Nevertheless, the intercellular distributions of MLCK1-EGFP and MLCK2-EGFP were distinct. MLCK1 was concentrated at the perijunctional actomyosin ring, where it colocalized with ZO-1 and, to a lesser degree, along lateral membranes (Fig. 2B, D, E). In contrast, MLCK2 was most prominently associated with lateral membranes and basal stress fibers and induced striking increases in stress fiber abundance

(Fig. 2B-F). Both the localization and functional impact of MLCK2 expression are, therefore, distinct from those of MLCK1.

MLCK1 interactions with the cytoskeleton are more stable than MLCK2 interactions

We and others have shown that MLCK-mediated MLC phosphorylation promotes F-actin polymerization (19-22) and that the enhanced F-actin polymerization induced by this regulated MLC activation can limit epithelial migration (23, 24). Given the striking differences in basal stress fiber density induced by MLCK2 overexpression, we asked if overexpression of either MLCK1 or MLCK2 affected epithelial migration. MLCK1-EGFP expression had no significant effect, but MLCK2 overexpression markedly inhibited cell migration (Fig. 3A). Together with preferential localization along stress fibers, this result suggests that MLCK2 is a primary effector of cytoskeletal regulation during epithelial migration.

Previous studies have shown that the affinity of MLCK1 for F-actin and myofilaments is greater than that of short, smooth muscle MLCK and this correlated with MLCK1-mediated stabilization of F-actin structures (25). We therefore asked whether MLCK1 and MLCK2 differed in their abilities to stabilize F-actin. To test this, monolayers were treated with latrunculin A (LatA), which reduced F-actin within cells expressing either MLCK1-EGFP or MLCK2-EGFP (Fig. 3B). However, MLCK1-EGFP-expressing monolayers retained significantly more F-actin than MLCK2-EGFP-expressing monolayers (Fig. 3B) after LatA treatment. MLCK1 therefore stabilizes microfilaments more effectively than MLCK2.

To determine the superiority of MLCK1 in stabilizing microfilaments reflected binding to the cytoskeleton, monolayers were imaged continuously after addition of a detergent-containing cytosolic extraction buffer. Both MLCK1-EGFP and MLCK2-EGFP were released following extraction. However, MLCK2-EGFP loss was significantly greater than that of MLCK1-EGFP (Fig. 3C). This result is not due to differential microfilaments stabilization, as F-actin content was not significantly reduced by cytosolic extraction of monolayers expressing either MLCK1-EGFP or MLCK 2-EGFP (Fig. 3C). Thus, MLCK1 is more stably associated with the cytoskeleton than MLCK2. Taken together with the distinct effects of LatA-induced F-actin depolymerization, these data suggest that interactions between microfilaments and MLCK1 are more stable than those with MLCK2.

The N-terminal extension that distinguishes long MLCK isoforms from smooth muscle MLCK is sufficient to direct MLCK1, but not MLCK2, to the perijunctional actomyosin ring

The short sequence encoded by exon 11 is the only difference between MLCK1 and MLCK2. This sequence completes IgCAM3 and has been suggested to be a substrate for Src kinase-mediated phosphorylation-induced increases in enzymatic capacity (6, 26). IgCAM3 is, however, distant from the C-terminal MLCK1 catalytic site. We therefore considered the hypothesis that subcellular localization differences between MLCK1 and MLCK2 are independent of enzymatic activity. To test this, we compared distributions of full-length MLCK1 and MLCK2 to those of truncated mutants continued only the first four IgCAM domains, MLCK1(IgCAM1-4) and MLCK2(IgCAM1-4). Similar to full-length MLCK1-EGFP, MLCK1(IgCAM1-4)-EGFP was concentrated at the perijunctional actomyosin ring at steady-state and recruited to the perijunctional actomyosin ring following TNF treatment (Fig. 3D, E). In contrast, neither MLCK2-EGFP nor MLCK2(IgCAM1-4)-EGFP were concentrated at the perijunctional actomyosin ring or redistributed following TNF stimulation (Fig. 3D, E). These data demonstrate that the IgCAM1-4 region of MLCK1 is both necessary and sufficient to direct basal and TNF-induced recruitment to the perijunctional actomyosin ring and further indicate that enzymatic activity is not required for MLCK1 localization.

MLCK1(IgCAM1-4) affinity for F-actin is greater than that of MLCK2(IgCAM1-4)

Previous work has identified an actin-binding region within the first two IgCAM domains of MLCK1 and MLCK2, which are identical (25, 27). Nevertheless, the preferential recruitment of MLCK1 and MLCK1(IgCAM1-4) to the perijunctional actomyosin ring, relative to MLCK2 and MLCK2(IgCAM1-4), suggests that the affinities of the MLCK1 and MLCK2 IgCAM1-4 regions for F-actin may differ. To assess this we performed spin-down assays using recombinant MLCK1(IgCAM1-4) and MLCK2(IgCAM1-4) and G-actin to evaluate G-actin sequestering, F-actin binding, and F-actin polymerization. MLCK1(IgCAM1-4) and MLCK2(IgCAM1-4) were equally soluble in the absence of actin (Fig. 4A). Further, both MLCK1(IgCAM1-4) and MLCK2(IgCAM1-4) enhanced F-actin polymerization and almost entirely co-sedimented with F-actin (Fig. 4A, B). Notably, the lack of polymerization inhibition suggests that neither protein binds significantly to G-actin. Moreover, kinetic analysis of G-actin polymerization confirmed that both MLCK1(IgCAM1-4) and MLCK2(IgCAM1-4) accelerated the rate and increased the final extent of F-actin polymerization similarly (Fig. 4C). Thus, despite substantial differences in

subcellular localization, there are no significant differences between MLCK1(IgCAM1-4) and MLCK2(IgCAM1-4) with respect to their effects on actin polymerization in vitro.

We also considered the possibility that the differences in affinities of MLCK1(IgCAM1-4) and MLCK2(IgCAM1-4) for F-actin might explain distinct subcellular localizations. To test this, we expressed MLCK1(IgCAM1-4) and MLCK2(IgCAM1-4) with C-terminal His tags as well as MLCK1(IgCAM3) (Fig. 5A) and analyzed their binding to F-actin by microscale thermophoresis. The Kd of MLCK1(IgCAM1-4) for F-actin was nearly half of that of MLCK2(IgCAM1-4), indicating a significantly greater affinity of MLCK1(IgCAM1-4) for F-actin (Fig. 5B, C). MLCK1(IgCAM3) did not bind well to F-actin, indicating that this single domain is insufficient to mediate F-actin binding in the absence of other IgCAMs (Fig. 5B, C).

Identification of the minimal MLCK1 targeting domain

The greater affinity of MLCK1(IgCAM1-4) for F-actin relative to that of MLCK2(IgCAM1-4) suggests that this could explain differential recruitment of MLCK1 and MLCK2 to the perijunctional actomyosin ring in polarized epithelial cells. To test this possibility, constructs identical to those studied in vitro were tagged with EGFP and stably expressed in intestinal epithelial cells (Fig. 6A). EGFP alone served as a control and was not significantly associated with the perijunctional actomyosin ring (Fig. 6B, C). Both MLCK1(IgCAM1-4) and MLCK2(IgCAM1-4) were present at the perijunctional actomyosin ring, but MLCK1(IgCAM1-4) recruitment was far greater than that of MLCK2(IgCAM1-4) (Fig. 6B, C). MLCK1(IgCAM1-3) recruitment was not significantly different than that of MLCK1(IgCAM1-4) (Fig. 6B, C). IgCAM3 alone failed to be recruited (Fig. 6B, C). Thus, the minimal MLCK1 recruitment domain is comprised of sequence from IgCAM1 to IgCAM3.

IgCAM3 acts as a dominant negative that limits TNF-induced MLCK1 recruitment and barrier loss

Although IgCAM3 alone was insufficient to direct targeting to the perijunctional actomyosin ring, the limited recruitment of MLCK2 constructs indicates that the complete IgCAM3 sequence is essential. We therefore hypothesized that the IgCAM3 domain could block critical interactions necessary for MLCK1 recruitment. To test this, cell lines with constitutive MLCK1-EGFP expression and inducible mCherry-IgCAM3 expression were created. Plating mixtures of these

cells showed that IgCAM3 significantly reduced MLCK1 recruitment to the perijunctional actomyosin ring (Fig. 7A, B). Moreover, IgCAM3 was able to completely block TNF-induced increases in MLCK1 recruitment (Fig. 7A, B). Thus, IgCAM3-mediated interactions are essential for both basal and TNF-induced MLCK1 recruitment to the perijunctional actomyosin ring.

We next asked whether mCherry-IgCAM3 expression affected barrier function. IgCAM3 expression resulted in a 38%±3% increase in steady-state TER (Fig. 7C). TNF was able to reduce TER of monolayers without or with mCherry-IgCAM3 expression, but the extent of TER loss was significantly reduced by mCherry-IgCAM3 expression ($P< 0.05$) (Fig. 7D). Thus, IgCAM3 expression limited TNF-induced barrier loss.

DISCUSSION

Our previous work using small molecules and dominant negative constructs has demonstrated that protein-protein interactions involving the IgCAM3 domain that differentiates MLCK1 from MLCK2 are viable therapeutic targets (6, 18). Specifically, we identified small molecules that bind directly to IgCAM3 or interfere with binding of an MLCK1 region that includes IgCAM3 to a chaperone protein and demonstrated that these molecules are able to reverse inflammation-induced barrier loss in vitro and in vivo (6, 18). While they emphasize the central importance of the MLCK1 IgCAM3 domain, these data do not demonstrate that IgCAM3 alone is sufficient to direct steady-state or inflammation-induced MLCK1 recruitment to the perijunctional actomyosin ring. Here, we sought to identify the minimal MLCK1 regions that direct this recruitment. Our data demonstrate that IgCAM3 alone can act as a dominant negative to prevent MLCK1 recruitment, but that a larger region including IgCAM2 is necessary for MLCK1 recruitment to the perijunctional actomyosin ring.

Long MLCK1 and MLCK2 differ only by the absence of a short 69 amino acid sequence in the latter (17). It is therefore possible to generate antibodies that selectively label MLCK1 but impossible to create MLCK2-specific antibodies. Thus, to analyze human tissue, we used antibodies specific for either MLCK1 or total long MLCK (MLCK1 and MLCK2). Importantly, neither of these antibodies labeled smooth muscle MLCK. Quantitative analysis showed that increased long MLCK expression in Crohn’s disease was largely a consequence of MLCK1 upregulation. Thus, consistent with its critical role in tight junction regulation, MLCK1 is specifically upregulated in ileal Crohn’s disease.

The mechanisms by which Crohn’s disease affects long MLCK mRNA splicing to favor MLCK1 are not defined. It is notable, however, that human SNPs rs77323602 and rs147245669 may favor generation of MLCK1 or MLCK2 transcripts, respectively, in endothelial cells (28, 29). In this context, heterogeneous nuclear ribonucleoprotein A1 (hnRNPA1) expression has been suggested to enhance splicing to remove exon 11 and generate MLCK2 transcripts (28, 29). In the intestine, hnRNPA1 is primarily expressed within undifferentiated epithelia (30), consistent with the preferential expression of MLCK2 by these cells (17). Although hnRNPA1 has not been studied in detail, previous work has linked the Crohn’s disease-associated 3020insC *NOD2* polymorphism to reduced hnRNPA1 splicing activity (31, 32). Thus, although further studies are needed, hnRNPA1 downregulation in Crohn’s disease could explain the shift that favors MLCK1 translation in disease.

We overcame the obstacle to developing MLCK2-specific antibodies by expressing EGFP-tagged MLCK1 and MLCK2 in intestinal epithelial cells. The distributions of these splice variants were remarkably different. MLCK1 was primarily localized to the perijunctional actomyosin ring. In contrast, MLCK2 was present at lateral membranes and within basal stress fibers that contained relatively little MLCK1. Moreover, MLCK2 overexpression increased the area covered by stress fibers and inhibited epithelial migration. Together with previous work, these data support the idea that MLCK2-mediated MLC phosphorylation enhances basal F-actin polymerization, increases stress fiber area, and interferes with the cytoskeletal dynamics required for migration (20-22, 33). Overall, these data show that the two long MLCK splice variants expressed in intestinal epithelium preferentially associate with and modulate different actin-rich structures to have distinct effects on epithelial function.

The striking differences between MLCK1 and MLCK2 are surprising given that these proteins differ by only 69 amino acids that comprise less than 4% of the primary sequence. Nevertheless, this sequence completes the IgCAM3 domain within the N-terminal extension that differentiates long from short MLCK proteins that are products of a single *MYLK* gene (34, 35). We therefore focused on the N-terminal extension to define the unique behaviors of MLCK1 and MLCK2. First, we showed that the IgCAM1-4 region of MLCK1, but not MLCK2, is sufficient to direct steady-state and TNF-induced recruitment to the perijunctional actomyosin ring. In addition to restricting the region that directs MLCK1 recruitment, these data indicate that enzymatic activity, which is not present in IgCAM1-4 constructs, is not required for recruitment. These results also indicate that the five F-actin-binding DXR motifs (25, 36) present within both MLCK1 and MLCK2 are not required for recruitment to the perijunctional actomyosin ring.

Previous studies have identified diverse functions for the IgCAM domains present within long MLCK, including recruitment to actin rich structures and in vitro binding to microfilaments (25, 27, 37, 38). IgCAM1-2 was reported to bind to F-actin in vitro with a Kd of 0.39 μM (27), similar to the ~0.50 μM Kd affinity we measured for MLCK2(IgCAM1-4) but somewhat greater than the 0.31 μM Kd affinity we measured for MLCK1(IgCAM1-4). We found that MLCK1(IgCAM1-3) binds to F-actin with a Kd of 0.43 μM, which was not significantly lower than that of MLCK2(IgCAM1-4) for F-actin. Results were quite different in living cells, where MLCK1(IgCAM1-3)-EGFP was recruited to the perijunctional actomyosin ring but MLCK2-EGFP was more prominently associated with stress fibers, similar to IgCAM1-2 (27). Together, the present data as well as previous reports by other groups and us indicate that, although IgCAM3

is required, recruitment to the perijunctional actomyosin ring is not simply reflective of F-actin binding affinity.

Despite binding F-actin poorly and failing to direct recruitment to the perijunctional actomyosin ring, IgCAM3 was an effective dominant inhibitor that displaced MLCK1 from the perijunctional actomyosin ring and increased barrier function at steady-state. IgCAM3 also blocked TNF-induced MLCK1 recruitment and limited barrier loss. This is consistent with our previous identification of a chaperone protein that binds to regions including IgCAM3 to direct MLCK1 recruitment as well as our demonstration that small molecules that disrupt IgCAM3-dependent interactions prevent MLCK1 recruitment and TNF-induced barrier loss (6, 18). Thus, while not sufficient, IgCAM3 is necessary for TNF-induced, MLCK1-mediated tight junction regulation.

As a whole, our data indicate that MLCK1 is preferentially upregulated in human Crohn's disease, where it is most concentrated within the perijunctional actomyosin ring of intestinal epithelial cells. In vitro studies identified the minimal MLCK1 region required for this perijunctional actomyosin ring recruitment and demonstrated the critical role of the IgCAM3 domain that distinguishes MLCK1 from MLCK2. Finally, we show that the MLCK1 IgCAM3 domain can act as a dominant negative inhibitor that prevents steady-state and TNF-induced MLCK1 recruitment and barrier regulation. Together, these data indicate that interactions mediated by IgCAM3 are both critical determinants of epithelial barrier regulation and rational targets for molecular therapeutic interventions.

MATERIALS AND METHODS

Human tissues

Human Crohn's disease patient biopsies were obtained from Brigham and Women's Hospital under IRB-approved protocols. Only well-oriented ileal biopsies with excellent tissue preservation were used. Biopsies with extensive ulceration were excluded. Small intestinal biopsies without abnormalities from age- and sex-matched healthy patients, e.g., undergoing screening colonoscopies, were used as controls. Formalin-fixed, paraffin-embedded biopsies were assembled into tissue microarrays prior to staining.

Cell lines

Plasmids with expression cassettes flanked by transposable elements were co-transfected with piggyBac transposase (System Biosciences) into clone 5E6L Caco-2_{BBe} cells. Expression cassettes encoded EGFP-tagged full length MLCK1 or MLCK2 as well as indicated mutants. Cells were also stably-transfected to express MLCK1-EGFP constitutively and mCherry-IgCAM3 inducibly via a Tet-on3G system (Clontech). Cells were maintained in high-glucose Dulbecco's modified Eagle's medium (Life Technologies) supplemented with 10% fetal calf serum, and 15 mM HEPES, pH 7.4, as previously-described (18, 39). Cells were treated with doxycycline (20 ng/ml) to induce mCherry-IgCAM3 expression.

For growth as polarized monolayers, Transwell inserts (Corning) were coated with rat tail collagen and plated as described (40). Cytokines were added basolaterally, with IFN-γ added 18 hours before TNF, which was added for 4 hours, as described (40).

For migration assays, cells were plated in 2 well inserts in µ-dish 35 mm plates (Ibidi). Inserts were removed to allow for migration over a defined area after cells within the wells became confluent.

Antibodies

Antigen affinity-purified rabbit anti-E-cadherin (Cell Signaling Technology, AB_2291471) was used for western blot (0.1 µg/ml); antigen affinity-purified rabbit anti-GFP (Novus, AB_523903) was used for western blot (2.2 µg/ml); antigen affinity-purified rabbit anti-long MLCK (AB_2921292) was used for immunofluorescence (10 µg/ml) and western blot (2.5 µg/ml); antigen affinity-purified rat anti-MLCK1 (AB_2909525) was used for immunofluorescence (20 µg/ml); monoclonal rat anti-ZO-1 (AB_2909525) was used for immunofluorescence (1 µg/ml); and mouse monoclonal anti-γ-actin (Santa Cruz, AB_2890619) was used for

immunofluorescence (0.4 µg/ml). Secondary antibodies conjugated to IRDye 680LT or IRDye 800CW (Li-Cor) were used for western blot and highly cross-adsorbed IgG $F(ab')_2$ secondary antibodies conjugated to Alexafluor 594 or Alexafluor 647 (Jackson Immunoresearch) were used for immunofluorescence.

Latrunculin A treatment and cytosolic extraction

Caco-2_{BBe} monolayers stably expressing EGFP-tagged MLCK1 and MLCK2 were equilibrated in HBSS for 30 min at 37 °C before the treatment. Then, the basolateral media was replaced by HBSS containing 1 µM LatA to allow actin depolymerization and cells were incubated at 37 °C (41). Monolayers were fixed before or 30 min after LatA treatment, stained for F-actin using Alexafluor 594 phalloidin, and imaged.

For extraction, cells were washed once with HBSS which was then removed and gently replaced with extraction buffer (50 mM MES, 3 mM EGTA, 5 mM $MgCl_2$, 0.5% Triton X-100, p H7.4), as described (42). Images were collected at time 0, and 2 and 4 min after CSK buffer treatment.

Electrophysiology

Monolayers were transferred from culture medium to HBSS supplemented with 15 mM HEPES, pH 7.4, and 25 mM D-glucose. After equilibration, potential differences were measured before and during application of a 50-µA current. Transepithelial short-circuit current (Isc) and transepithelial resistance (TER) were calculated using Ohm's law, as previously described (2, 43).

Immunostains

Formalin-fixed, paraffin-embedded ileal samples from age-sex matched Crohn's patients and healthy controls were assembled into tissue microarrays. Sections were deparaffinized and rehydrated and underwent antigen retrieval using Trilogy (Sigma-Aldrich) solution and a pressure cooker. After cooling, sections were incubated in bleaching buffer under a bright LED (broad spectrum) light for 1 hour at room temperature (44). After replenishing with fresh bleaching buffer, incubation under light was continued for an additional 1 hour. After incubation with blocking buffer (Agilent), primary antibodies prepared in antibody diluent (Agilent) were added for 8 hours at room temperature. After 5 washes, secondary antibodies with Hoechst

33342 (1 µg/ml) were added for 1 hour. After washing, sections were mounted using Vectashield Plus Antifade Medium (Vector Laboratories).
Caco-2_{BBe} cells were fixed in 1% paraformaldehyde-lysine-periodate fixative (45) and immunostained as described previously. F-actin was stained with Alexafluor 594 phalloidin.

Imaging

Widefield imaging was performed using an Axioplan 2 widefield microscope (Zeiss) with 20x NA 0.8 Plan-Apochromat and 100x NA 1.4 Plan-Neofluar objectives, ET filter cubes (Chroma), LED illuminator (Lumencor SOLAO), and Coolsnap HQ (Photometrics) camera controlled by MetaMorph 7 (Molecular Devices). Confocal images were obtained using a DM6000 microscope (Leica) with a CSU-X1 spinning disk (Yokogawa), 100x NA 1.4 HC PLAN APO CS2 objective, emission filters (Semrock), 4-channel solid-state Borealis laser launch (Andor), and Zyla 4.2 Plus sCMOS camera (Andor) controlled by MetaMorph. Enhanced resolution images used a Zeiss LSM 880 with Airyscan and a Plan-Apochromat 63X/1.40 Oil DIC M27 objective. The super resolution mode was used using 0.16 µm/pixel, 1024 x 1024 frame size, 2x averaging, and 4x digital zoom.
Tiled tissue microarray images were collected using a DM4000 widefield microscope with 20X NA 0.7 HC PLAN APO objective (Leica), ORCA-Flash 4.0 LT+ CMOS camera (Hamamatsu), motorized emission filter wheel and xyz stage (Ludl), 5 channel Aura light engine (Lumencor), and multichannel dichroic matched to single band excitation filters (Semrock), controlled by MetaMorph 7, as described (44).

Post-acquisition analysis and morphometry

Post-acquisition processing and analysis used MetaMorph 7 (Molecular Devices), Autoquant X3 (MediaCybernetics), FIJI (46), and Imaris 9.9.0 (Bitplane). For MLCK1 and total MLCK analysis in human biopsies, quantitative morphometry was performed using Cell Profiler (47). Villus and crypt regional masks with whole biopsy tiled scans were created manually, and whole epithelial and apical epithelial masks were generated based on γ-actin distribution. Intensities were normalized to γ-actin after preliminary validation showing that γ-actin expression was unchanged in Crohn’s disease.
For analysis of cultured cells, the perijunctional actomyosin ring was defined based on phalloidin staining. ImageJ (National Institutes of Health, Bethesda, MD, USA) was used to create a region of interest (ROI) around the complete cell and a discrete intracellular ROI. The larger ROI was taken as total fluorescence. The fluorescence of the smaller ROI was subtracted from total and

then normalized to total fluorescence to determine the perijunctional MLCK fraction (6). For analysis of stress fiber area, Zeiss Airyscan images were rendered using IMARIS 9.9.0. The Imaris surface function was used in tandem with the machine learning classification and the FIJI Labkit plugin.

Recombinant protein preparation, actin polymerization, and microscale thermophoresis

His-tagged recombinant proteins were expressed in Rosetta2 (DE3)pLysS bacteria (Novagen) and purified on IMAC columns (Bio-Rad) using an AktaPure FPLC system (Cytiva). Purity was assessed by SDS-PAGE.

Actin binding and polymerization were assessed using the actin binding protein kit (Cytoskeleton, BK013). Actin pellet gel bands were quantified by densitometry using FIJI.

In vitro actin polymerization was assessed using the actin polymerization kit (Cytoskeleton, BK003). Briefly, 60 µL of 4.53 µM pyrene-labelled G-actin was polymerized in presence or absence of 2 µM MLCK1(IgCAM1-4) or MLCK2(IgCAM1-4). Fluorescence was monitored using a Synergy H1 (Biotek) plate reader at excitation and emission wavelengths of 365 and 407 nm, respectively.

His-tagged MLCK proteins were labeled using a His-Tag Labeling Kit RED-tris-NTA (NanoTemper). Microscale thermophoresis was performed using a Monolith NT.115 (NanoTemper). Data were analyzed by MO Affinity Analysis software. F-actin was polymerized from chicken gizzard (smooth muscle) muscle actin (Cytoskeleton, APHL99).

Statistics

All data are presented as mean ± SD and are representative of at least 3 independent experiments. Statistical significance was determined by 2-tailed Student's *t* test (unpaired) or 1-way ANOVA with Bonferroni's correction, as indicated in each figure legend using GraphPad Prism 9. *, $P < 0.05$; **, $P < 0.01$; ***, $P < 0.001$.

Acknowledgments: We thank Drs. W Vallen Graham, Yi-Tang Wang, and Harry Rosenberg for their contributions to early phases of this work, Dr. Nitesh Shashikanth and Dr. Jose Yeste for their assistance with confocal microscopy and image processing, Dr. Kelly L. Arnett and the Harvard Center for Macromolecular Interactions for instruction and assistance with microscale thermophoresis, Dr. Lay-Hong Ang for instruction and assistance with Airyscan microscope, and Heather Marlett (Nationwide Histology) for outstanding tissue preparation.

REFERENCES

1. Zolotarevsky Y*, et al.* (2002) A membrane-permeant peptide that inhibits MLC kinase restores barrier function in in vitro models of intestinal disease *Gastroenterol.* 123:163-172.
2. Turner JR*, et al.* (1997) Physiological regulation of epithelial tight junctions is associated with myosin light-chain phosphorylation *Am. J. Physiol.* 273:C1378-1385.
3. Clayburgh DR*, et al.* (2005) Epithelial myosin light chain kinase-dependent barrier dysfunction mediates T cell activation-induced diarrhea in vivo *J. Clin. Invest.* 115:2702-2715.
4. Su L*, et al.* (2013) TNFR2 activates MLCK-dependent tight junction dysregulation to cause apoptosis-mediated barrier loss and experimental colitis *Gastroenterol.* 145:407-415.
5. Su L*, et al.* (2009) Targeted epithelial tight junction dysfunction causes immune activation and contributes to development of experimental colitis *Gastroenterol.* 136:551-563.
6. Graham WV*, et al.* (2019) Intracellular MLCK1 diversion reverses barrier loss to restore mucosal homeostasis *Nat. Med.* 25:690-700.
7. Ma TY, Boivin MA, Ye D, Pedram A, & Said HM (2005) Mechanism of TNF-alpha modulation of Caco-2 intestinal epithelial tight junction barrier: role of myosin light-chain kinase protein expression *Am. J. Physiol. - Gastrointest. Liver Physiol.* 288:G422-430.
8. Wang F*, et al.* (2005) Interferon-gamma and tumor necrosis factor-alpha synergize to induce intestinal epithelial barrier dysfunction by up-regulating myosin light chain kinase expression *Am. J. Pathol.* 166:409-419.
9. Al-Sadi R, Ye D, Dokladny K, & Ma TY (2008) Mechanism of IL-1beta-induced increase in intestinal epithelial tight junction permeability *J. Immunol.* 180:5653-5661.
10. Feighery LM*, et al.* (2008) Myosin light chain kinase inhibition: correction of increased intestinal epithelial permeability in vitro *Pharm. Res.* 25:1377-1386.
11. Chen C, Wang P, Su Q, Wang S, & Wang F (2012) Myosin light chain kinase mediates intestinal barrier disruption following burn injury *PLoS One* 7:e34946.
12. Guo M*, et al.* (2012) Role of non-muscle myosin light chain kinase in neutrophil-mediated intestinal barrier dysfunction during thermal injury *Shock* 38:436-443.
13. Zahs A*, et al.* (2012) Inhibition of long myosin light-chain kinase activation alleviates intestinal damage after binge ethanol exposure and burn injury *Am. J. Physiol. - Gastrointest. Liver Physiol.* 303:G705-712.

14. Lorentz CA*, et al.* (2017) Myosin light chain kinase knockout improves gut barrier function and confers a survival advantage in polymicrobial sepsis *Mol Med* 23:155-165.
15. Nalle SC*, et al.* (2019) Graft-versus-host disease propagation depends on increased intestinal epithelial tight junction permeability *J. Clin. Invest.* 129:902-914.
16. Pai YC*, et al.* (2020) Gut microbial transcytosis induced by tumor necrosis factor-like 1A-dependent activation of a myosin light chain kinase splice variant contributes to IBD *Journal of Crohn's & colitis* 15:258–272.
17. Clayburgh DR*, et al.* (2004) A differentiation-dependent splice variant of myosin light chain kinase, MLCK1, regulates epithelial tight junction permeability *J. Biol. Chem.* 279:55506-55513.
18. Zuo L*, et al.* (2022) Tacrolimus-binding protein FKBP8 directs myosin light chain kinase-dependent barrier regulation and is a potential therapeutic target in Crohn's disease *Gut* gutjnl-2021-326534.
19. Chen X, Pavlish K, & Benoit JN (2008) Myosin phosphorylation triggers actin polymerization in vascular smooth muscle *Am. J. Physiol. - Heart Circ. Physiol.* 295:H2172-2177.
20. Shen L*, et al.* (2006) Myosin light chain phosphorylation regulates barrier function by remodeling tight junction structure *J. Cell Sci.* 119:2095-2106.
21. Goeckeler ZM & Wysolmerski RB (1995) Myosin light chain kinase-regulated endothelial cell contraction: the relationship between isometric tension, actin polymerization, and myosin phosphorylation *J Cell Biol* 130:613-627.
22. Katoh K, Kano Y, Amano M, Kaibuchi K, & Fujiwara K (2001) Stress fiber organization regulated by MLCK and Rho-kinase in cultured human fibroblasts *Am. J. Physiol. - Cell Physiol.* 280:C1669-1679.
23. Schmidt JT, Morgan P, Dowell N, & Leu B (2002) Myosin light chain phosphorylation and growth cone motility *J. Neurobiol.* 52:175-188.
24. Chen C*, et al.* (2014) Myosin light chain kinase (MLCK) regulates cell migration in a myosin regulatory light chain phosphorylation-independent mechanism *J. Biol. Chem.* 289:28478-28488.
25. Smith L*, et al.* (2002) Properties of long myosin light chain kinase binding to F-actin in vitro and in vivo *J. Biol. Chem.* 277:35597-35604.
26. Birukov KG*, et al.* (2001) Differential regulation of alternatively spliced endothelial cell myosin light chain kinase isoforms by p60(Src) *J. Biol. Chem.* 276:8567-8573.

27. Yang CX*, et al.* (2006) Microfilament-binding properties of N-terminal extension of the isoform of smooth muscle long myosin light chain kinase *Cell Res* 16:367-376.
28. Mascarenhas JB*, et al.* (2017) Mechanical stress and single nucleotide variants regulate alternative splicing of the MYLK gene *Am. J. Respir. Cell Mol. Biol.* 56:29-37.
29. Mascarenhas JB*, et al.* (2018) The splicing factor hnRNPA1 regulates alternate splicing of the MYLK gene *Am. J. Respir. Cell Mol. Biol.* 58:604-613.
30. Karlsson M*, et al.* (2021) A single-cell type transcriptomics map of human tissues *Sci Adv* 7.
31. Noguchi E, Homma Y, Kang X, Netea MG, & Ma X (2009) A Crohn's disease-associated NOD2 mutation suppresses transcription of human IL10 by inhibiting activity of the nuclear ribonucleoprotein hnRNP-A1 *Nat. Immunol.* 10:471-479.
32. Clarke JP, Thibault PA, Salapa HE, & Levin MC (2021) A comprehensive analysis of the role of hnRNP A1 function and dysfunction in the pathogenesis of neurodegenerative disease *Front Mol Biosci* 8:659610.
33. Turner JR & Basson MD (2002) Roles of the extracellular matrix and cytoskeleton in intestinal epithelial restitution. *Gastrointestinal Mucosal Repair and Experimental Therapeutics*, eds Hob CH & Wang JY (Karger Press), pp 1-13.
34. Lazar V & Garcia JG (1999) A single human myosin light chain kinase gene (MLCK; MYLK) *Genomics* 57:256-267.
35. Kamm KE & Stull JT (2001) Dedicated myosin light chain kinases with diverse cellular functions *J. Biol. Chem.* 276:4527-4530.
36. Poperechnaya A, Varlamova O, Lin PJ, Stull JT, & Bresnick AR (2000) Localization and activity of myosin light chain kinase isoforms during the cell cycle *J Cell Biol* 151:697-708.
37. Dulyaninova NG, Patskovsky YV, & Bresnick AR (2004) The N-terminus of the long MLCK induces a disruption in normal spindle morphology and metaphase arrest *J. Cell Sci.* 117:1481-1493.
38. Zhang WC*, et al.* (2008) Identification and functional characterization of an aggregation domain in long myosin light chain kinase *FEBS J* 275:2489-2500.
39. Buschmann MM*, et al.* (2013) Occludin OCEL-domain interactions are required for maintenance and regulation of the tight junction barrier to macromolecular flux *Mol. Biol. Cell* 24:3056-3068.

40. Pongkorpsakol P, Turner JR, & Zuo L (2020) Culture of intestinal epithelial cell monolayers and their use in multiplex macromolecular permeability assays for in vitro analysis of tight junction size selectivity *Curr Protoc Immunol* 131:e112.
41. Shen L & Turner JR (2005) Actin depolymerization disrupts tight junctions via caveolae-mediated endocytosis *Mol. Biol. Cell* 16:3919-3936.
42. Zhao H*, et al.* (2004) Ezrin regulates NHE3 translocation and activation after Na+-glucose cotransport *Proc. Natl. Acad. Sci. U.S.A.* 101:9485-9490.
43. Shashikanth N, Rizzo HE, Pongkorpsakol P, Heneghan JF, & Turner JR (2021) Electrophysiologic analysis of tight junction size and charge selectivity *Curr Protoc* 1:e143.
44. Abtahi S*, et al.* (2021) A simple method for creating a high-content microscope for imaging multiplexed tissue microarrays *Curr Protoc* 1:e68.
45. McLean IW & Nakane PK (1974) Periodate-lysine-paraformaldehyde fixative. A new fixation for immunoelectron microscopy *J. Histochem. Cytochem.* 22:1077-1083.
46. Schindelin J*, et al.* (2012) Fiji: an open-source platform for biological-image analysis *Nat Methods* 9:676-682.
47. McQuin C*, et al.* (2018) CellProfiler 3.0: Next-generation image processing for biology *PLoS Biol* 16:e2005970.

Figure 1

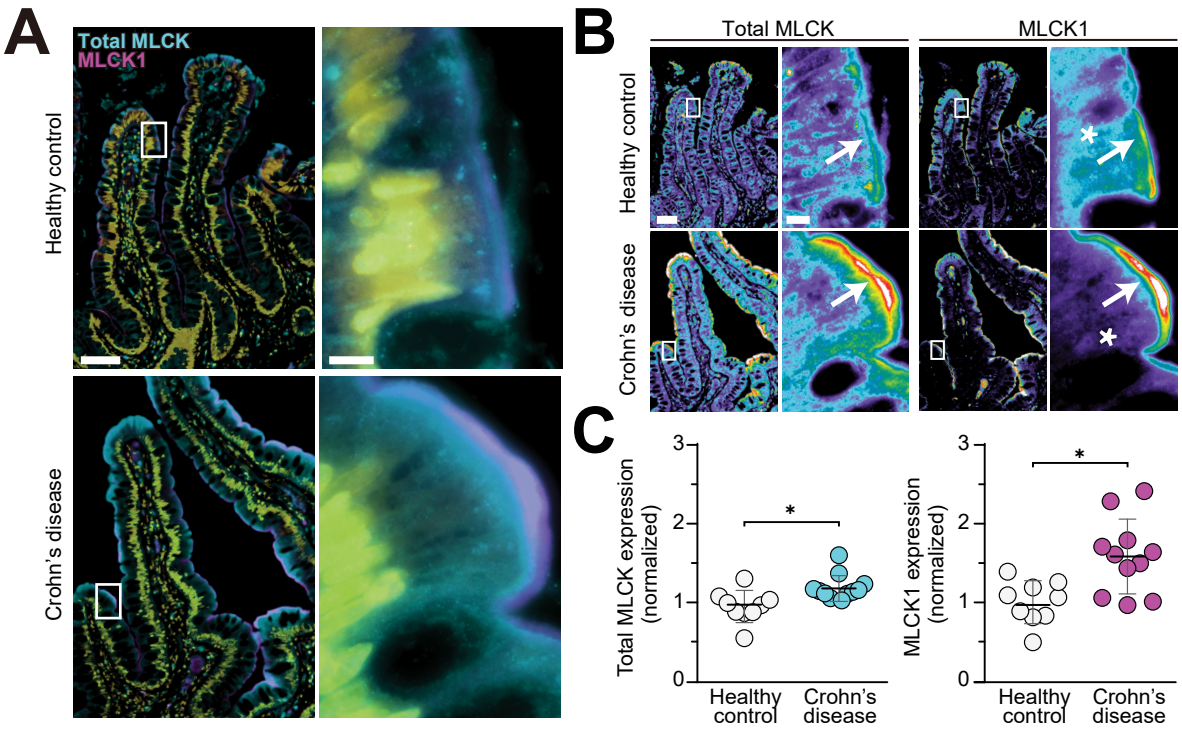
A
Total MLCK
MLCK1
Healthy control
Crohn's disease
B
Total MLCK
MLCK1
Healthy control
Crohn's disease
C
Total MLCK expression (normalized)
MLCK1 expression (normalized)
0
1
2
3
*
Healthy control
Crohn's disease

Figure 1. MLCK1 expression and perijunctional actomyosin ring recruitment are specifically increased in Crohn's disease. **A.** Representative immunostains of ileal biopsies from Crohn's disease patients and healthy controls labeled for long MLCK1 (magenta), total long MLCK (cyan), and nuclei (yellow). Note the dense MLCK1 band at the perijunctional actomyosin ring in Crohn's disease. In contrast, the perijunctional actomyosin ring contains relatively little MLCK1 in healthy control tissues. Bars = 50 μm, 5 μm. **B.** Total MLCK or MLCK1 pseudocolor heatmap images of the same fields as A. The small amount of MLCK1 expressed in healthy controls is present at the perijunctional actomyosin ring (arrow) and within the cytoplasm (asterisk). In contrast, MLCK1 expression in Crohn's disease is almost exclusively within the perijunctional actomyosin ring (arrow), and there is little cytoplasmic staining (asterisk). Note the overall increase in total MLCK expression and perijunctional localization (arrow) in Crohn's disease. Bars = 50 μm, 5 μm. **C.** Quantitative morphometry of total MLCK and MLCK1 staining in individual biopsies. Each point represents a distinct patient. n = 9 healthy controls, n = 11 Crohn's disease patients. Mean ± SD. Student's t test. *, $P < 0.05$.

Figure 2

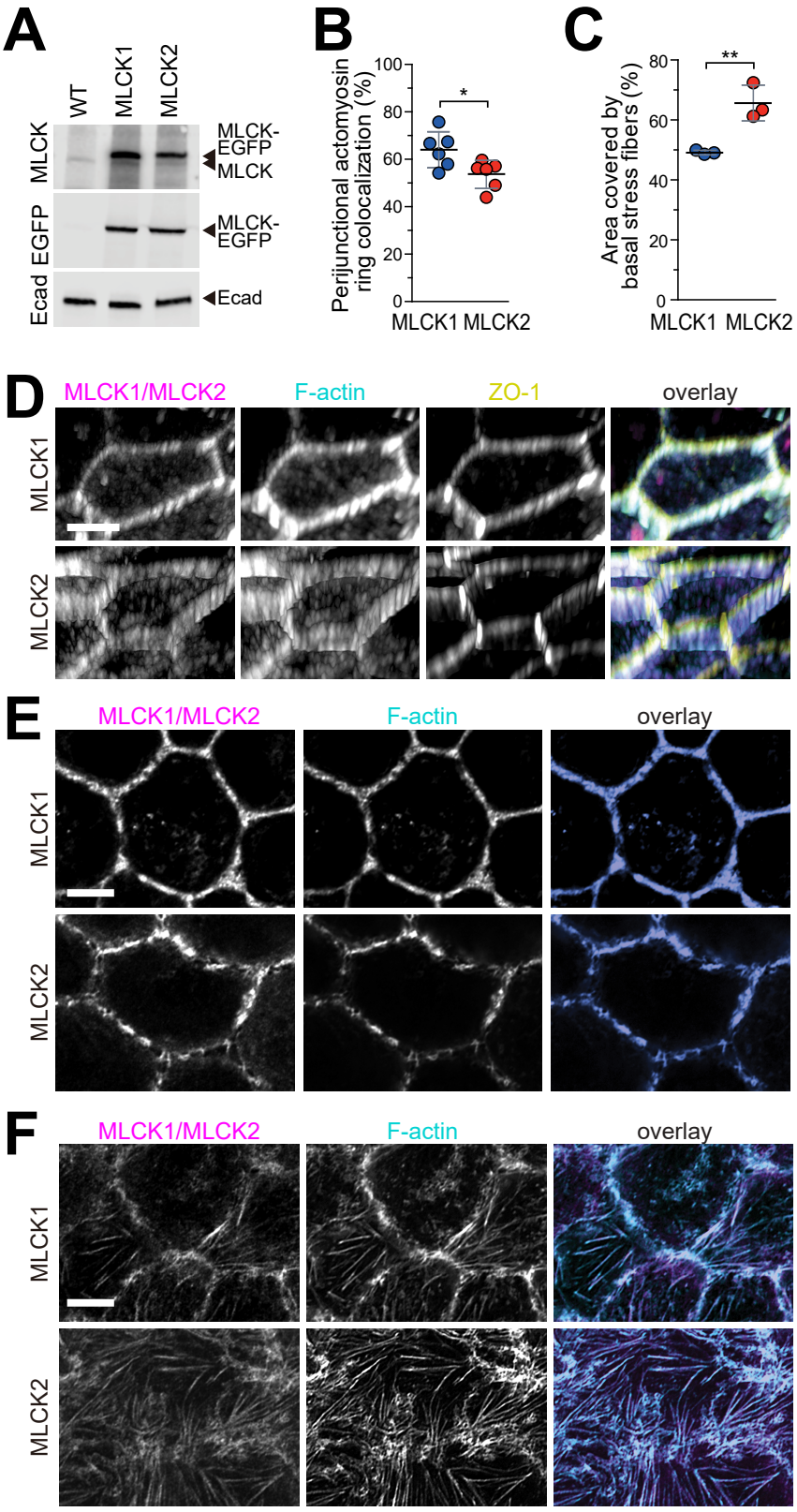
A
WT
MLCK1
MLCK2
MLCK
EGFP
Ecad
MLCK-EGFP
MLCK
MLCK-EGFP
Ecad
B
Perijunctional actomyosin ring colocalization (%)
100
80
60
40
20
0
*
MLCK1 MLCK2
C
Area covered by basal stress fibers (%)
80
60
40
20
0
**
MLCK1 MLCK2
D
MLCK1/MLCK2
F-actin
ZO-1
overlay
MLCK1
MLCK2
E
MLCK1/MLCK2
F-actin
overlay
MLCK1
MLCK2
F
MLCK1/MLCK2
F-actin
overlay
MLCK1
MLCK2

Figure 2. MLCK1 and MLCK2 have distinct intracellular distributions. **A.** Western blot analysis of wild type (WT) or stably-transfected Caco-2_{BBe} monolayers. Cells expressing MLCK1-EGFP (MLCK1) or MLCK2-EGFP (MLCK2) have similar transgene expression, and both represent overexpression relative to endogenous long MLCK. **B.** Quantitative morphometry demonstrates preferential localization of MLCK1-EGFP (MLCK1), relative to MLCK2-EGFP (MLCK2), within the perijunctional actomyosin ring. $n = 6$. Mean ± SD. Student's *t* test. *, $P < 0.05$. **C.** MLCK2-EGFP (MLCK2) overexpression increased basal stress fiber density relative to MLCK1-EGFP overexpressing or WT monolayers. $n = 3$. Mean ± SD. Student's *t* test. **, $P < 0.01$. **D.** 3D projections showing subcellular localization of MLCK1-EGFP (MLCK1, magenta) or MLCK2-EGFP (MLCK2, magenta) as well as F-actin (cyan) and ZO-1 (yellow). Note the close colocalization of EGFP-MLCK1 with ZO-1. In contrast, EGFP-MLCK2 is prominent at lateral membranes below the tight junction. Bar = 3 μm. **E.** Airyscan confocal slices at the level of the perijunctional actomyosin ring demonstrate a dense, nearly continuous, ring of MLCK1-EGFP with little cytoplasmic signal. In contrast, EGFP-MLCK2 is less dense, discontinuous, and present within a cloud of faint staining adjacent to the perijunctional actomyosin ring. Bar = 3 μm. **F.** Airyscan confocal slices at the level of the basal stress fibers show colocalization of both MLCK1-EGFP and MLCK2-EGFP with F-actin. However, both the number of stress fibers and the intensity with which they are decorated by MLCK2-EGFP are greater than those of MLCK1-EGFP. Bar = 3 μm.

Figure 3

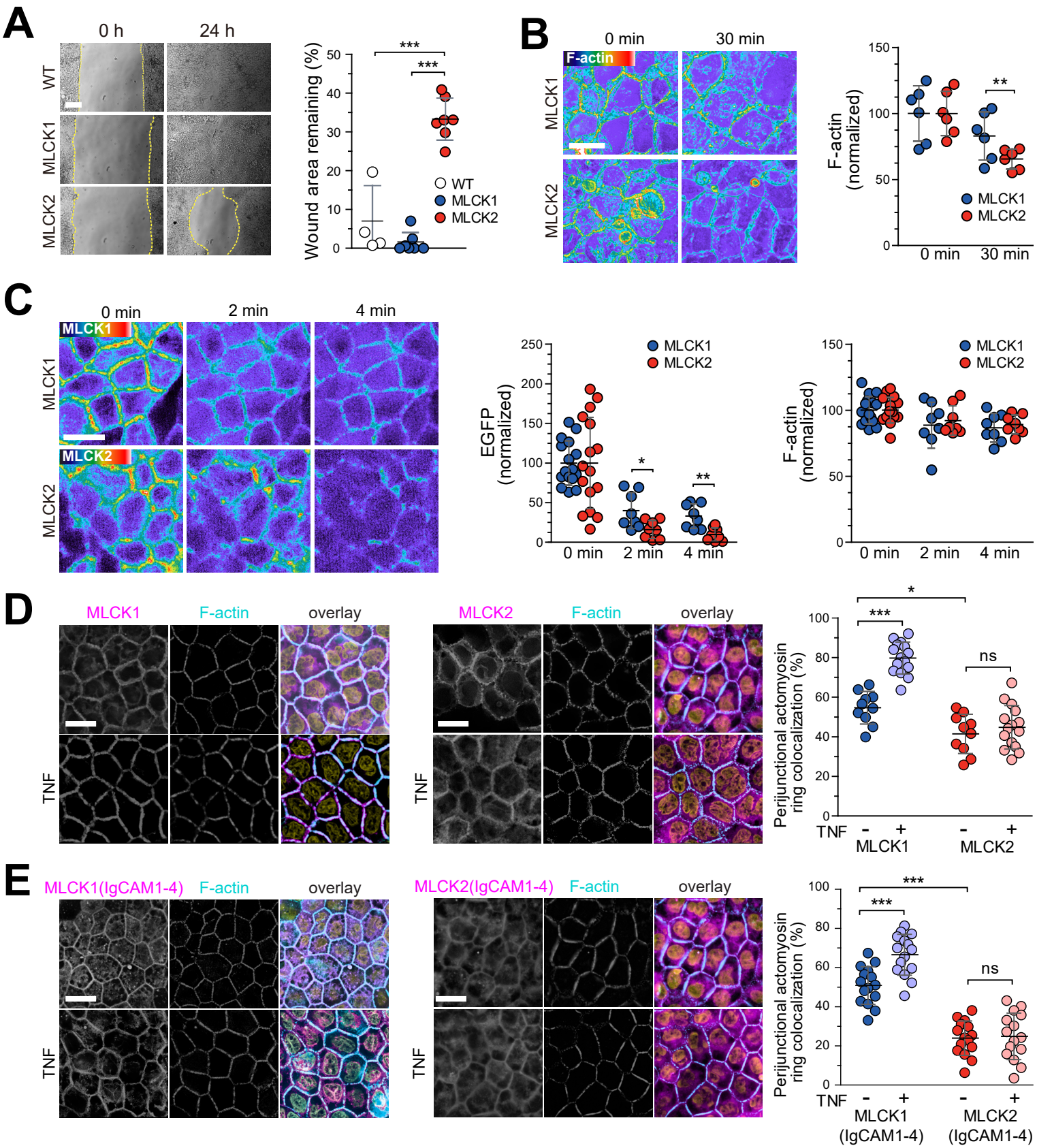
A
0 h
24 h
WT
MLCK1
MLCK2
Wound area remaining (%)
***
***
WT
MLCK1
MLCK2
B
0 min
30 min
F-actin
MLCK1
MLCK2
F-actin (normalized)
**
MLCK1
MLCK2
0 min
30 min
C
0 min
2 min
4 min
MLCK1
MLCK2
EGFP (normalized)
*
**
F-actin (normalized)
D
MLCK1
F-actin
overlay
MLCK2
TNF
Perijunctional actomyosin ring colocalization (%)
*
***
ns
TNF
MLCK1
MLCK2
E
MLCK1(IgCAM1-4)
MLCK2(IgCAM1-4)
MLCK1 (IgCAM1-4)
MLCK2 (IgCAM1-4)

Figure 3. Divergent behaviors of MLCK1 and MLCK2. **A.** MLCK1-EGFP (MLCK1) overexpression does not impact epithelial migration relative to wild type (WT). In contrast, MLCK2-EGFP (MLCK2) overexpression markedly delays migration. Representative images are shown. Bar = 100 μm. *n* = 4-7. Mean ± SD. ANOVA. ***, P < 0.001. **B.** Representative pseudocolor heatmap images show F-actin staining before and 30 min after treatment of monolayers expressing MLCK1-EGFP (MLCK1) or MLCK2-EGFP (MLCK2) with LatA (1 μM). MLCK1-EGFP stabilized perijunctional F-actin. Bar = 10 μm. *n* = 6. Mean ± SD. Student's *t* test. **, P < 0.01. **C.** Monolayers expressing MLCK1-EGFP (MLCK1) or MLCK2-EGFP (MLCK2) were extracted with detergent-containing buffer. Representative pseudocolor heatmap images collected at 2 minute intervals are shown. MLCK1-EGFP was better retained than MLCK2-EGFP. Parallel samples were fixed and stained for F-actin, which was similar in both sets of monolayers. Bar = 10 μm. *n* = 8 - 16. Mean ± SD. Student's *t* test. *, P < 0.05. **, P < 0.01. **D, E** Caco-2_{BBe} monolayers with stable expression of MLCK1-EGFP (MLCK1), MLCK2-EGFP (MLCK2), MLCK1(IgCAM1-4)-EGFP (MLCK1(IgCAM1-4)), or MLCK2(IgCAM1-4)-EGFP (MLCK2(IgCAM1-4)) were treated with TNF, as indicated, for 4 hrs. EGFP-type constructs (magenta), F-actin (cyan), and nuclei (yellow) are shown in the overlay images. Morphometric analyses showed that IgCAM1-4 truncation mutants are or are not recruited to the perijunctional actomyosin ring similar to corresponding full-length MLCK constructs. Bars = 10 μm. *n* = 10 - 15. Mean ± SD. ANOVA. *, P <0.05. ***, P <0.001.

Figure 4

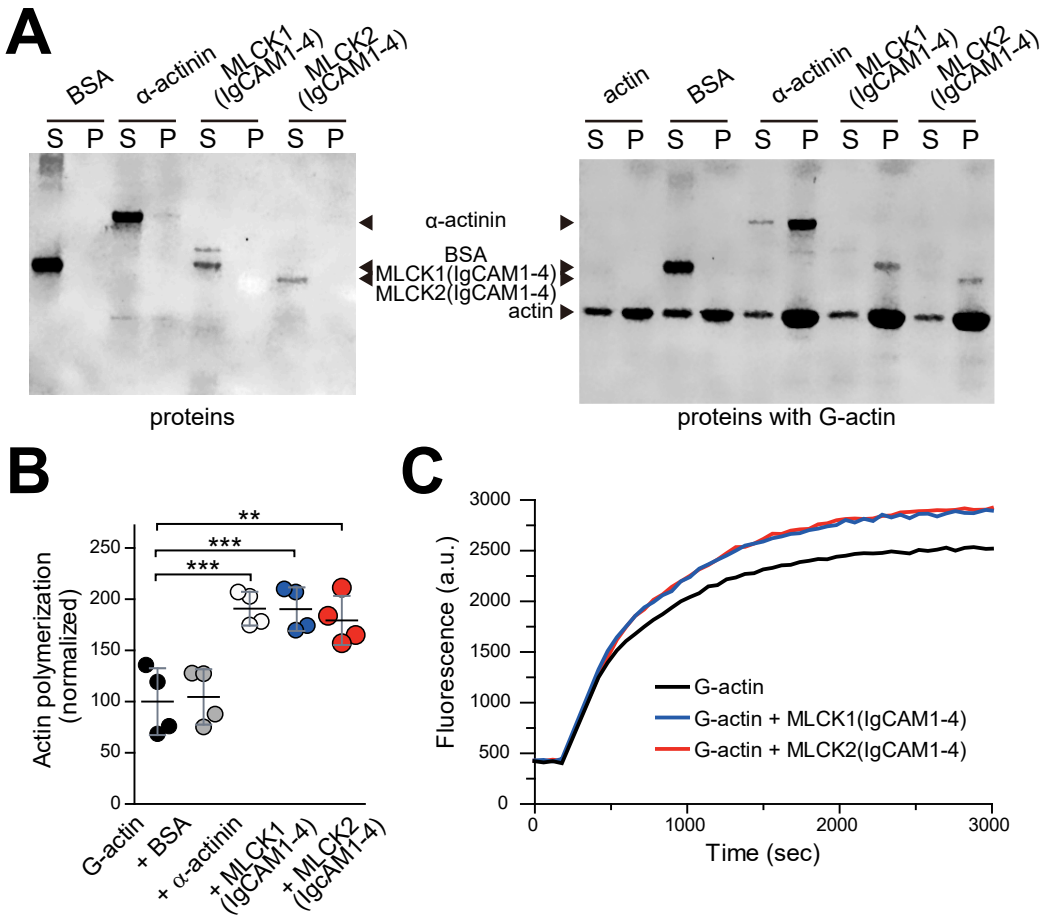
A
BSA
α-actinin
MLCK1 (IgCAM1-4)
MLCK2 (IgCAM1-4)
S P S P S P S P
α-actinin
BSA
MLCK1(IgCAM1-4)
MLCK2(IgCAM1-4)
actin
proteins
actin
BSA
α-actinin
MLCK1 (IgCAM1-4)
MLCK2 (IgCAM1-4)
S P S P S P S P S P
proteins with G-actin
B
Actin polymerization (normalized)
0
50
100
150
200
250
**
***
***
G-actin
+ BSA
+ α-actinin
+ MLCK1 (IgCAM1-4)
+ MLCK2 (IgCAM1-4)
C
Fluorescence (a.u.)
0
500
1000
1500
2000
2500
3000
Time (sec)
0
1000
2000
3000
G-actin
G-actin + MLCK1(IgCAM1-4)
G-actin + MLCK2(IgCAM1-4)

Figure 4. MLCK1(IgCAM1-4) and MLCK2(IgCAM1-4) promote actin polymerization. **A.** Spin-down assays were performed to assess actin binding and polymerization enhancement activity. In the absence of added G-actin (left), bovine serum albumin (BSA, 66 kD), α-actinin (100 kD), MLCK1(IgCAM1-4) (67 kD), and MLCK2(IgCAM1-4) (59 kD) are all found within the supernatant (S) fraction. When incubated with G-actin (right) before centrifugation, BSA remains in the supernatant and does not affect the amount of polymerized F-actin found in the pellet (P) relative to control without added protein. In contrast, α-actinin, MLCK1(IgCAM1-4), and MLCK2(IgCAM1-4) all enhanced actin polymerization and were sequestered within the F-actin pellet. **B.** Quantitative analysis showing increased F-actin polymerization in the presence of α-actinin, MLCK1(IgCAM1-4), or MLCK2(IgCAM1-4), but not BSA. n = 4 Mean ± SD. ANOVA. **, P <0.01. ***, P <0.001. **C.** Pyrene-labeled G-actin polymerization was monitored by fluorescence. Both MLCK1(IgCAM1-4) and MLCK2(IgCAM1-4) accelerated the extent of polymerization. Traces shown are representative of n = 3 in this experiment.

Figure 5

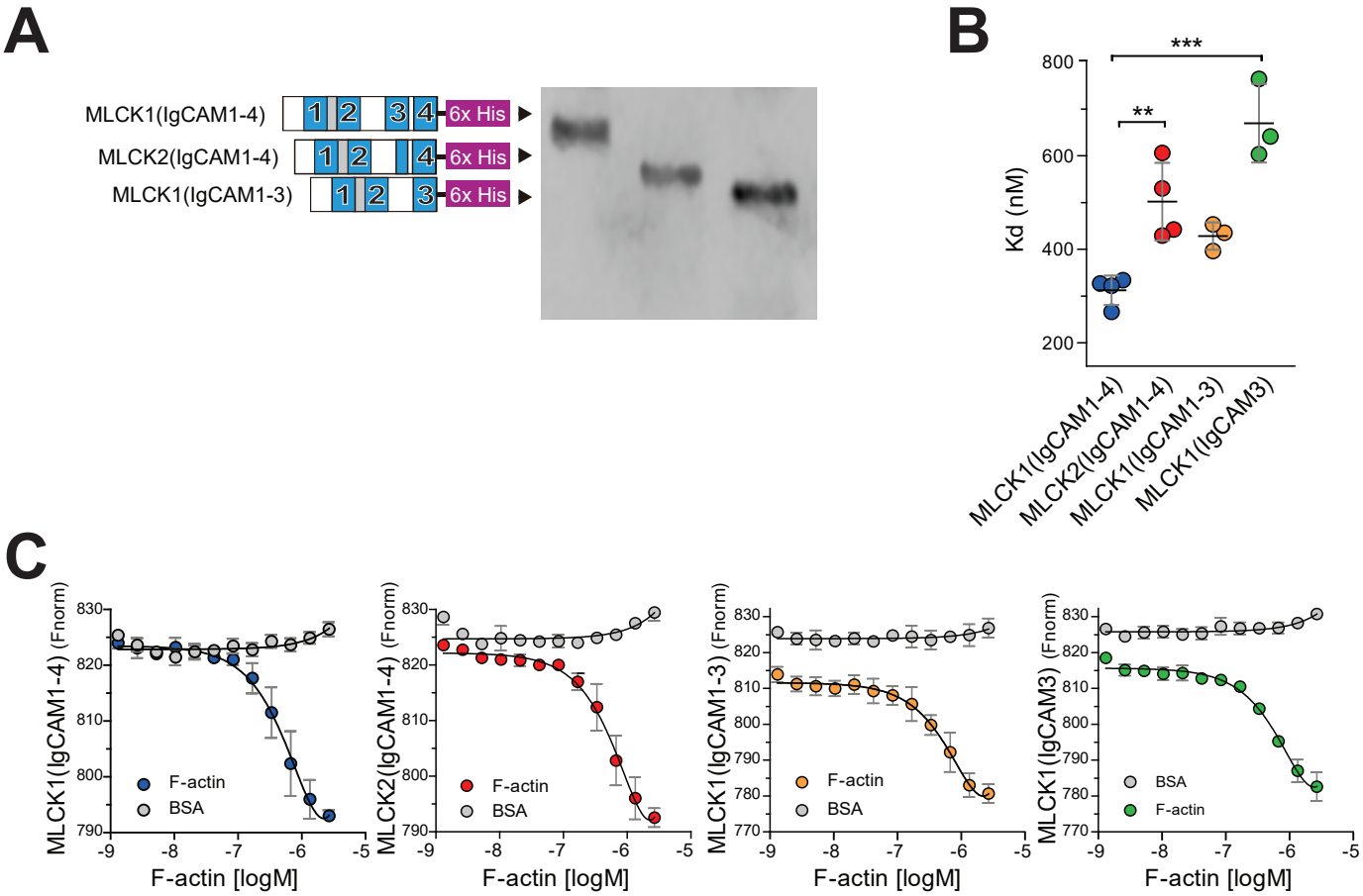
A
MLCK1(IgCAM1-4)
MLCK2(IgCAM1-4)
MLCK1(IgCAM1-3)
1
2
3
4
6x His
B
Kd (nM)
800
600
400
200
***
**
MLCK1(IgCAM1-4)
MLCK2(IgCAM1-4)
MLCK1(IgCAM1-3)
MLCK1(IgCAM3)
C
MLCK1(IgCAM1-4) (Fnorm)
MLCK2(IgCAM1-4) (Fnorm)
MLCK1(IgCAM1-3) (Fnorm)
MLCK1(IgCAM3) (Fnorm)
F-actin
BSA
F-actin [logM]

Figure 5. F-actin binds MLCK1 with greater affinity than MLCK2. **A.** Structures and SDS-PAGE analysis of His-tagged recombinant MLCK constructs used for microscale thermophoresis (MST) assays. IgCAM domains are numbered and shown in blue. The short sequence between the end of IgCAM1 and the beginning of IgCAM2 is shown in gray. **B.** Dissociation constants (Kd) of MLCK protein construct-binding to F-actin. *n* = 3-4. Mean ± SD. ANOVA. **, P <0.01. ***, P <0.001. **C.** Representative binding curves of unlabeled F-actin with 10 nM indicated his tag-labeled recombinant MLCK protein. BSA binding (grey circles) was used as a negative F-actin binding control for each construct. His tag-labeled human serum albumin (pink circles) did not bind to F-actin (target binding control).

Figure 6

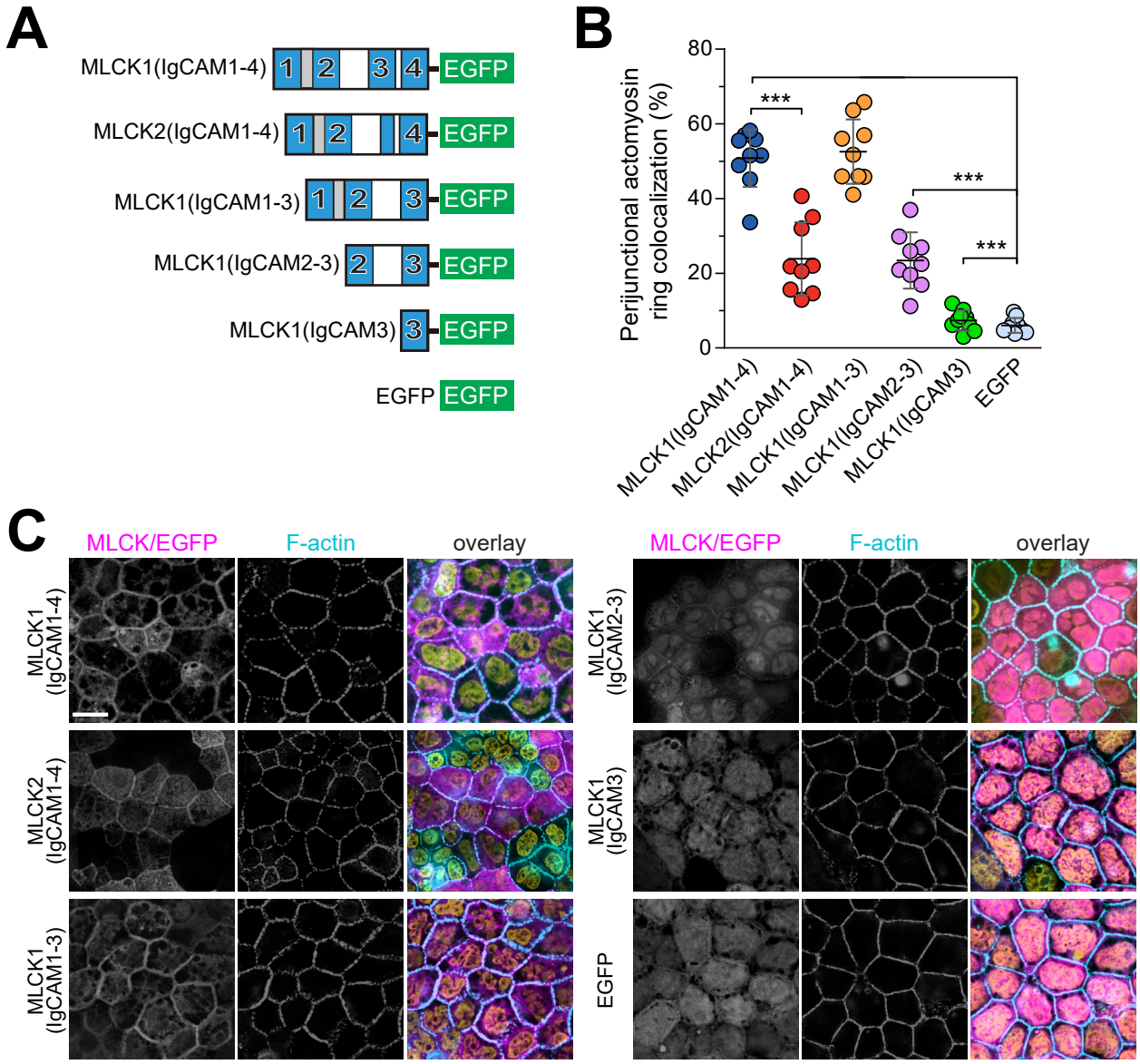
A
MLCK1(IgCAM1-4)
MLCK2(IgCAM1-4)
MLCK1(IgCAM1-3)
MLCK1(IgCAM2-3)
MLCK1(IgCAM3)
EGFP
B
Perijunctional actomyosin ring colocalization (%)
80
60
40
20
0
***
***
***
MLCK1(IgCAM1-4)
MLCK2(IgCAM1-4)
MLCK1(IgCAM1-3)
MLCK1(IgCAM2-3)
MLCK1(IgCAM3)
EGFP
C
MLCK/EGFP
F-actin
overlay
MLCK1 (IgCAM1-4)
MLCK2 (IgCAM1-4)
MLCK1 (IgCAM1-3)
MLCK1 (IgCAM2-3)
MLCK1 (IgCAM3)
EGFP

Figure 6. IgCAM 2-3 as well as the unstructured sequences preceding these domains is the minimal region required for steady-state MLCK1 trafficking. **A.** Structures and SDS-PAGE analysis of EGFP-tagged MLCK constructs stably expressed in Caco-2_{BBe} cells. IgCAM domains are numbered and shown in blue. The short sequence between the end of IgCAM1 and the beginning of IgCAM2 is shown in gray. Free EGFP was stably expressed as a negative control. **B.** Quantitative morphometry of perijunctional actomyosin ring localization of MLCK constructs. *n* = 9. Mean ± SD. ANOVA. ***, P <0.001. **C.** Representative images of EGFP-tagged MLCK constructs or EGFP (magenta), F-actin (cyan), and nuclei (yellow). Bar = 10 μm.

Figure 7

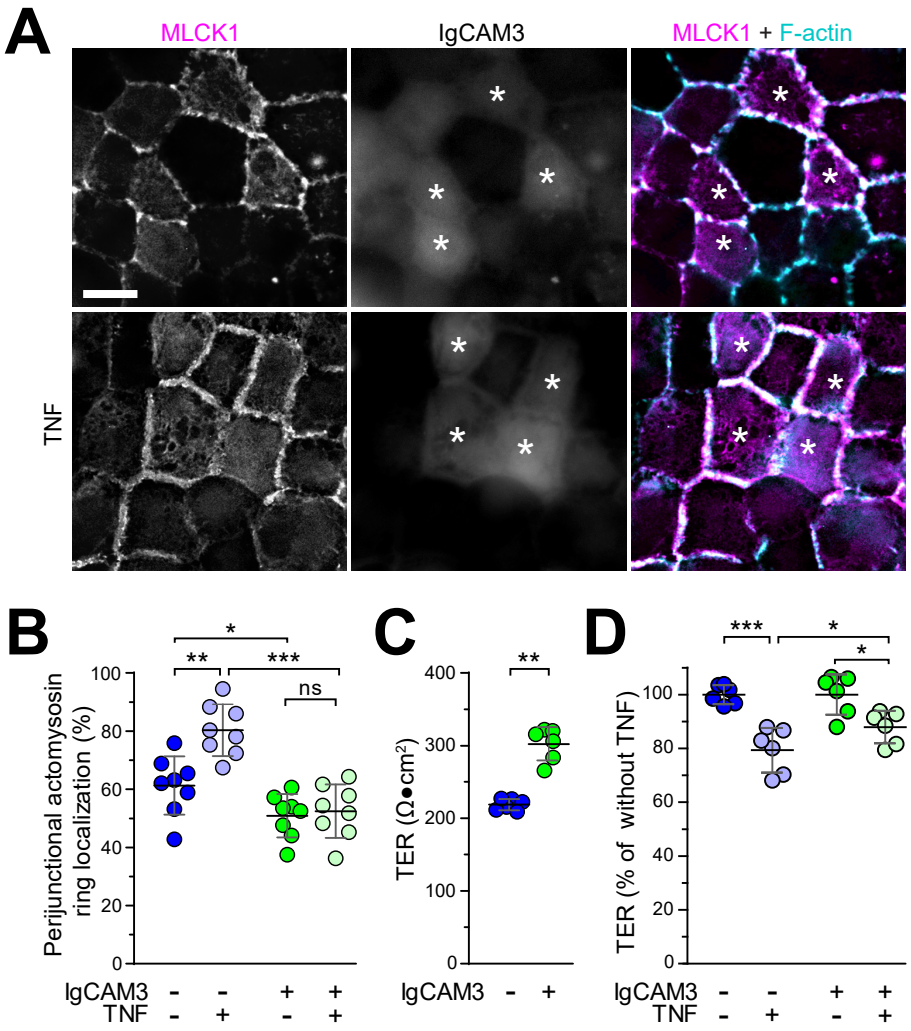
A
MLCK1
IgCAM3
MLCK1 + F-actin
TNF
B
Perijunctional actomysosin ring localization (%)
IgCAM3
TNF
ns
C
TER (Ω•cm²)
IgCAM3
D
TER (% of without TNF)
IgCAM3
TNF

Figure 7. IgCAM3 acts as a dominant negative to block TNF-induced MLCK1 trafficking. **A.** Caco-2_{BBe} monolayers expressing MLCK1-EGFP (MLCK1) with and without mCherry-IgCAM3 expression. IgCAM3 expression (asterisks) increased cytoplasmic MLCK1 before and after TNF treatment. The overlay shows MLCK1 (magenta) and F-actin (cyan). Bar = 10 μm.
B. Morphometric analysis of perijunctional MLCK1 in the absence (blue symbols) or presence (green symbols) of mCherry-IgCAM3 expression before (dark symbols) or after (light symbols) TNF treatment. *n* = 8. Mean ± SD. ANOVA. *, P < 0.05. **, P <0.01. ***, P <0.001. **C.** Transepithelial electrical resistance (TER) measurement of MLCK1-EGFP-expressing monolayers at steady-state without (blue symbols) or with (green symbols) mCherry-IgCAM3 expression. *n*= 6. Mean ± SD. Student's *t* test. **, P < 0.01. **D.** TER of MLCK1-EGFP-expressing monolayers without (blue symbols) or with (green symbols) inducible mCherry-IgCAM3 expression. TER after TNF treatment (light symbols) is normalized to TER of similar monolayers before TNF treatment (dark symbols). *n* = 6. Mean ± SD. ANOVA. *, P <0.01, ***, P <0.001.